Uniaxial rebound at the nematic biaxial transition

Fulvio Bisi
Dipartimento di Matematica and CNISM, Università di Pavia, via Ferrata 1, I-27100 Pavia, Italy

Silvano Romano
Dipartimento di Fisica "A. Volta" and CNISM, Università di Pavia, via A. Bassi 6, I-27100 Pavia, Italy

Epifanio G. Virga
Dipartimento di Matematica and CNISM, Università di Pavia, via Ferrata 1, I-27100 Pavia, Italy
(Received 13 November 2006; revised manuscript received 20 January 2007; published 24 April 2007)

Over the last few years, renewed interest has been raised by the simplified general interaction models proposed by Straley for mesogenic molecules possessing the D_{2h} symmetry and capable of producing biaxial nematic order. It has already been shown that, in the presence of certain special symmetries, just two out of the four order parameters that are in general necessary, suffice for the description of a biaxial phase. For some other range of parameters, these reducing symmetries do not hold, and, moreover, a mean-field treatment has to be suitably changed into a minimax strategy, still producing a transition to a low-temperature biaxial phase. Upon studying the general parameter range, we identify as a common feature the behavior of a uniaxial order parameter, attaining a local minimum at the biaxial-to-uniaxial transition temperature, and recognizably increasing away from it. This finding is confirmed by a Monte Carlo simulation.

DOI: 10.1103/PhysRevE.75.041705 PACS number(s): 61.30.Cz, 61.30.Dk

I. INTRODUCTION

Nematic biaxial phases, predicted theoretically by Freiser [1,2], in thermotropic liquid crystals, have proved far more elusive than anticipated. Since Yu and Saupe's [3] first experimental proof of their existence in lyotropic liquid crystals, the meandering history of their search in thermotropics has experienced many rough turns and more than one delusion [4]. Though the recent announcement of a series of independent observations of these phases [5–10] has raised considerable interest among liquid crystal experts [11], these experimental results have not yet met with unanimous consensus [12–14].

Theoretically, the existence of thermotropic biaxial phases is supported by many predictions, based on both analytical and computational methods. A detailed bibliography can be found, for example, in [15], and here only a few among the relevant papers will be quoted. We record, for later reference, the mean-field model originally put forward by Straley [16,17] and the detailed Monte Carlo simulation performed by Biscarini *et al.* [18] for a particular—though largely employed—instance of Straley's pair-potential, related to the London dispersion forces approximation [19]. Hard-core (excluded-volume) models have been investigated as well, both by analytical theories (usually Onsager-type treatments) and simulation, and have been found capable of predicting a biaxial phase for appropriate choices of potentials [20–24]. Another mean-field model was also built upon a different realization of Straley's pair-potential [25,26]; it revealed, among other aspects, the possibility for the direct isotropic-to-biaxial transition to take place over a full range of model parameters, instead of a single one, as within the dispersion forces approximation. Moreover, according to this model the transition to the biaxial phase from both isotropic and uniaxial phases can be either first- or second-order, depending on the choice of a model parameter [27,28]. Such a variety of behaviors resulted from varying a single parameter of the two allowed by the general form of Straley's pair potential. The dispersion forces approximation represents a similar reduction of Straley's pair potential, but this and the one put forward by Sonnet *et al.* [25] are accompanied by different features of the phase diagram. Straley's general pair potential was recently studied [29] for all inequivalent choices of the model parameters [30].

In the dispersion forces approximation, the pair potential takes the form of the inner product between two molecular biaxial tensors, one pertaining to each of the interacting molecules [54]. Such a form, which we also call a London *attractor*, embodies the tendency of two adjacent molecules to lie one parallel to the other, side-by-side, as it were. This special form of Straley's interaction is characteristic of dispersion forces approximation. When this approximation is abandoned, however, Straley's interaction Hamiltonian H can still be decomposed as the sum of two London interactions, but they need not be both attractors [29]. The region of admissible Straley's parameters is divided in two subregions by the curve—a parabola, in our parametrization—corresponding to the dispersion forces approximation: in one region, H is the sum of two London attractors, in the other region, H is the sum of a London attractor and a London *repulsor*, that is, a London interaction promoting skew relative orientations between adjacent molecules. We call *fully attractive* a Hamiltonian in the former region and *partly repulsive* a Hamiltonian in the latter region. In particular, the quadrupolar projection of the exact excluded-volume interaction for spherocuboids, a family of hard particles that include both platelets and spheroplatelets as special cases [31–34], is partly repulsive [35].

Both fully attractive and partly repulsive Hamiltonians were found to give rise to the same sequence of condensed phases [29], with essentially the same phase diagram as the one derived by Sonnet *et al.* [25], which was thus recognized

as universal. Upon lowering the temperature, the isotropic phase can either suffer a direct transition to the biaxial phase or this can be preceded by an intermediate uniaxial phase. While the isotropic-to-uniaxial transition is always first-order, all other transitions can be either first- or second-order, depending on the choice of the interaction parameters.

Four scalar order parameters are in general needed to describe a biaxial phase: in our terminology [25] they were denoted as (S,T,S',T'), where S is Maier and Saupe's original uniaxial parameter [36]. When both T and T' vanish, the phase is uniaxial, when either T or T' grows away from zero, the phase is biaxial, but the biaxiality has different origins in the two cases: it arises from the lack of rotational symmetry in the distribution of the long molecular axis when $T\neq 0$, while it arises from a tendency toward alignment of the short molecular axes when $T'\neq 0$. Similarly, S and S' express different measures of uniaxiality, the latter being induced by the alignment of the short molecular axes. Different authors have named differently the four scalar order parameters that describe a biaxial nematic phase: a rather complete account on the diversity of the notation and an attempt to establish conversion rules between them were recently presented by Rosso [37].

The interaction we have most studied so far [25,28] is characterized by symmetry properties [30] that eventually result in a reduction of the number of order parameters. It was shown that two order parameters would then suffice to describe the whole variety of stable condensed phases for this class of biaxial nematics [38]. Similar reductions are not known for a generic interaction.

This paper seeks a generic, unifying feature for the order parameter profiles. Our outcomes will complement the universal sequence of stable equilibrium phases [29]. We apply the mean-field model that has already been employed in previous studies [25,28–30]. Special attention will be given to the region in the parameter space where the interaction Hamiltonian is partly repulsive, as there the mean-field free energy fails to possess a global minimum in the order parameter space, and the search for the stable phases is conducted through a minimax principle, proposed in a different context by Bogolubov [39–41].

The class of interaction potentials employed here is outlined in Sec. II. Our mean-field model is briefly recalled in Sec. III, and the desired unifying feature is accordingly identified in Sec. IV. In Sec. V, we present the outcomes of computer simulations performed for selected partly repulsive Hamiltonians. Our main conclusions are summarized in the final Sec. VI.

II. MOLECULAR INTERACTION

A biaxial molecule possesses the same symmetry as a parallelepiped. Let $\boldsymbol{e}$, $\boldsymbol{e}_\perp$, and $\boldsymbol{m}$ denote the axes around which the molecule is invariant under rotations by an angle π (see Fig. 1). This is often referred to as the D_{2h} symmetry. Conventionally, we say that $\boldsymbol{m}$ is the long molecular axis, which would play the role of the molecular director, were the molecule uniaxial around it, in which case one would say that the molecule enjoys the $D_{\infty h}$ symmetry. It is easily seen

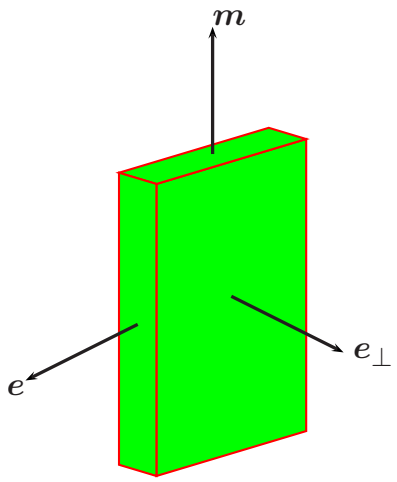

FIG. 1. (Color online) A biaxial molecule can be pictured as a brick; $\boldsymbol{e}$, $\boldsymbol{e}_\perp$, and $\boldsymbol{m}$ denote the axes around which the molecule is invariant under rotations by an angle π.

[37] that all symmetric, traceless tensors enjoying the D_{2h} symmetry about the molecular axes $(\boldsymbol{e},\boldsymbol{e}_\perp,\boldsymbol{m})$ can be written as linear combinations of

$$\mathbf{q} := \boldsymbol{m}\otimes\boldsymbol{m} - \frac{1}{3}\mathbf{I} \quad \text{and} \quad \mathbf{b} := \boldsymbol{e}\otimes\boldsymbol{e} - \boldsymbol{e}_\perp\otimes\boldsymbol{e}_\perp, \tag{1}$$

where $\mathbf{I}$ is the identity tensor. Thus the anisotropic part of any molecular susceptibility can be written as a linear superposition of these tensors.

Assuming within a dispersion model that these components interact separately with one another, one can justify the general form given by Straley [16] to the spatial average [55] of the interaction Hamiltonian:

$$H = -U_0\{\xi\mathbf{q}\cdot\mathbf{q}' + \gamma(\mathbf{q}\cdot\mathbf{b}' + \mathbf{b}\cdot\mathbf{q}') + \lambda\mathbf{b}\cdot\mathbf{b}'\}, \tag{2}$$

where $U_0>0$ is a scaling energy, and ξ, γ, and λ are scalar parameters, any of which can be chosen with unit modulus, with no loss of generality. In Eq. (2) the two interacting molecules are represented by the pairs of tensors $(\mathbf{q},\mathbf{b})$ and $(\mathbf{q}',\mathbf{b}')$.

In [38] we chose $|\xi|=1$ and we showed that, to within a permutation of axes and a possible rescaling of U_0, all different Hamiltonians in Eq. (2) that attain their minimum in the configuration where the interacting molecules lay parallel to one another, side by side, are represented by $\xi=1$ and (γ,λ) in the *essential* triangle defined by the inequalities

$$\gamma \geqslant 0, \quad \lambda \geqslant 0, \quad 1-2\gamma-3\lambda \geqslant 0, \tag{3}$$

which is depicted in Fig. 2. The vertices O, I, and V have the following coordinates in the (γ,λ) plane: $\mathsf{O}=(0,0)$, $\mathsf{I}=(0,\frac{1}{3})$, and $\mathsf{V}=(\frac{1}{2},0)$.

For $\lambda=\gamma^2$, Eq. (2) reduces to the Hamiltonian H_0 put forward by Freiser [1,2], in accordance with the classical London dispersion forces approximation:

$$H_0 := -U_0\mathbf{a}\cdot\mathbf{a}', \tag{4}$$

where $\mathbf{a}:=\mathbf{q}+\gamma\mathbf{b}$ and $\mathbf{a}':=\mathbf{q}'+\gamma\mathbf{b}'$ are the anisotropic parts of the dielectric susceptibility tensors of the interacting mol-

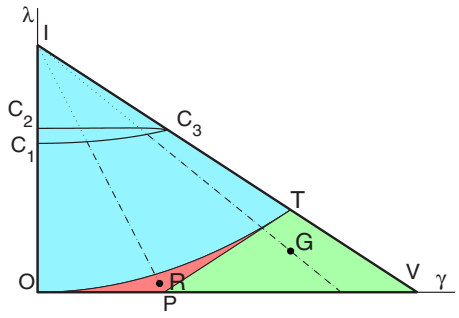

FIG. 2. (Color online) The *essential* triangle in the (γ,λ) plane; this region, defined by the inequalities (3), is sufficient to represent all different Hamiltonians in Eq. (2), to within a permutation of axes and a possible rescaling of U_0. The coordinates of the vertices are the following: $\mathsf{O}=(0,0)$, $\mathsf{I}=(0,\frac{1}{3})$, and $\mathsf{V}=(\frac{1}{2},0)$. $\mathsf{C}_1\mathsf{C}_3$ is a tricritical line: the corresponding phase diagram exhibits a tricritical point along the uniaxial-to-biaxial transition. $\mathsf{C}_2\mathsf{C}_3$ is a triple line: the corresponding phase diagram exhibits a single direct isotropic-to-biaxial transition, where the isotropic, uniaxial, and biaxial phases are in equilibrium [29]. The coordinates of the limiting points of these lines are the following: $\mathsf{C}_1\simeq(0,0.20)$, $\mathsf{C}_2\simeq(0,0.22)$, and $\mathsf{C}_3=(\frac{5}{29},\frac{19}{87})$. The arc OT is a portion of the dispersion parabola $\lambda=\gamma^2$. PT is the intersection of the essential triangle with the line tangent to this parabola at T. PT divides the region below the dispersion parabola, corresponding to partially repulsive Hamiltonians, into two sectors; a point was chosen within each sector, as illustrated in the text. These points are $\mathsf{R}=(\frac{\sqrt{3}}{3}-\frac{5}{12},\frac{7}{6}-\frac{2\sqrt{3}}{3})$ and $\mathsf{G}=(\frac{1}{3},\frac{1}{18})$.

ecules. For $\gamma=0$, H reduces to the Hamiltonian studied in [25,28]. In the essential triangle, this special Hamiltonian is represented by the segments OI and IT with $\mathsf{T}=(\frac{1}{3},\frac{1}{9})$, whereas H_0 is represented by the arc OT along the parabola $\lambda=\gamma^2$. Both points O and T are somewhat peculiar: while the former corresponds to a Hamiltonian H_0 with **a** uniaxial, the latter corresponds to a Hamiltonian H_0 with **a** bearing the largest possible biaxiality, as $\det \mathbf{a}=0$. All other points along the arc OT represent different blends of these pure interaction states.

In Fig. 2, the segment PT with $\mathsf{P}=(\frac{1}{6},0)$ is tangent to the dispersion parabola at T. It is shown in [38] that the triangle PTV is special within the essential triangle, as it is its only subregion mapped onto the plane $\xi=-1$ by a permutation symmetry. That is, when $\xi=-1$, so that the long molecular axes would repel each other, there is an axis permutation that transforms the Hamiltonian H into another where the transformed long axes attract each other again; the transformed Hamiltonian is described by a point within the triangle PTV.

The arc OT divides the essential triangle into two subregions: in both, H can be decomposed in the sum of two terms resembling H_0:

$$H = -U_0\{a^+\mathbf{q}^+\cdot\mathbf{q}^{+\prime}+a^-\mathbf{q}^-\cdot\mathbf{q}^{-\prime}\}, \tag{5}$$

where $\mathbf{q}^+$ and $\mathbf{q}^-$ are linear combinations of $\mathbf{q}$ and $\mathbf{b}$ depending on both γ and λ. While in OTI both a^+ and a^- are positive, in OTV they have oppostite sign [29]. Thus in OTI both diagonal terms in Eq. (5) are attractive, whereas in OTV one is attractive and the other is repulsive, though H remains globally attractive.

This different behavior of H in OTI and OTV is reflected in calling H *fully attractive* in the former region and *partly repulsive* in the latter. The difference between these Hamiltonians is not just in their names: as shown in [29], when associated with a fully attractive Hamiltonian, the mean-field free energy possesses a global minimum, whereas it fails to do so when associated with a partly repulsive Hamiltonian. A minimax principle was proposed and justified in [29] to tackle partly repulsive Hamiltonians within the mean-field approximation.

III. MEAN-FIELD TREATMENT

All condensed phases that an ensemble of biaxial molecules can manifest are represented by the order tensors defined by [25]

$$\mathbf{Q} := \langle\mathbf{q}\rangle \text{ and } \mathbf{B} := \langle\mathbf{b}\rangle, \tag{6}$$

where the ensemble average $\langle\cdots\rangle$ will here be computed within the mean-field approximation [25,29]. Both $\mathbf{Q}$ and $\mathbf{B}$ are symmetric and traceless by construction. In the absence of any external distorting cause that would disrupt their D_{2h} symmetry, they share one and the same eigenframe [37], and so they can be represented as

$$\mathbf{Q} = S\left(\boldsymbol{e}_z\otimes\boldsymbol{e}_z-\frac{1}{3}\mathbf{I}\right)+T(\boldsymbol{e}_x\otimes\boldsymbol{e}_x-\boldsymbol{e}_y\otimes\boldsymbol{e}_y), \tag{7a}$$

$$\mathbf{B} = S'\left(\boldsymbol{e}_z\otimes\boldsymbol{e}_z-\frac{1}{3}\mathbf{I}\right)+T'(\boldsymbol{e}_x\otimes\boldsymbol{e}_x-\boldsymbol{e}_y\otimes\boldsymbol{e}_y). \tag{7b}$$

In this representation of a condensed phase, S and S' are uniaxial order parameters, whereas T and T' are biaxial. When these latter vanish, while both S and S' do not, both $\mathbf{Q}$ and $\mathbf{B}$ are uniaxial tensors and so is the phase they describe, even if S and S' have a different meaning, the latter being related to the anisotropy in the distribution of the short molecular axes $\boldsymbol{e}$ and $\boldsymbol{e}_\perp$. Likewise, of the two biaxial parameters T and T', the latter is related to the molecular biaxiality, while the former characterizes the lack of rotational symmetry in the distribution of the long molecular axis $\boldsymbol{m}$ [25,28].

The scalar order parameters (S,T,S',T') must obey four consistency conditions, equivalent to the stationarity conditions for the free energy $\mathcal{F}$ defined as

$$\mathcal{F} = U_0\left\{\frac{1}{3}S^2+T^2+2\gamma\left(\frac{1}{3}SS'+TT'\right)+\lambda\left(\frac{1}{3}S'^2+T'^2\right)-\frac{1}{\beta}\ln\left(\frac{Z}{8\pi^2}\right)\right\}, \tag{8}$$

where

$$\frac{1}{\beta} := \frac{k_Bt}{U_0} \tag{9}$$

is the reduced temperature, k_B is the Boltzmann constant, and Z is the partition function. In the parametrization of the molecular orientation adopted in [25],

$$\boldsymbol{m} = (\cos\varphi \sin\vartheta)\boldsymbol{e}_x + (\sin\varphi \sin\vartheta)\boldsymbol{e}_y + (\cos\vartheta)\boldsymbol{e}_z,$$

$$\boldsymbol{e} = (\cos\psi\cos\varphi\cos\vartheta - \sin\psi\sin\varphi)\boldsymbol{e}_x + (\cos\psi\sin\varphi\cos\vartheta + \sin\psi\cos\varphi)\boldsymbol{e}_y - (\cos\psi\sin\vartheta)\boldsymbol{e}_z,$$

$$\boldsymbol{e}_\perp = -(\sin\psi\cos\varphi\cos\vartheta + \cos\psi\sin\varphi)\boldsymbol{e}_x - (\sin\psi\sin\varphi\cos\vartheta - \cos\psi\cos\varphi)\boldsymbol{e}_y + (\sin\psi\sin\vartheta)\boldsymbol{e}_z. \tag{10}$$

Here ϑ, φ, and ψ represent the polar angle, the azimuth, and the angle of proper rotation, respectively. In these variables,

$$Z = \int_0^{2\pi}\int_0^{2\pi}\int_{-1}^{1} \exp(\beta g)\,du\,d\varphi\,d\psi, \tag{11}$$

where $u := \cos\vartheta$ and

$$g := \mathbf{q}\cdot\mathbf{Q} + \gamma(\mathbf{q}\cdot\mathbf{B} + \mathbf{b}\cdot\mathbf{Q}) + \lambda\mathbf{b}\cdot\mathbf{B} = \left(u^2 - \frac{1}{3}\right)(S + \gamma S') + (1-u^2)[(T+\gamma T')\cos 2\varphi + (\gamma S + \lambda S')\cos 2\psi] + [(1+u^2)\cos 2\varphi\cos 2\psi - 2u\sin 2\varphi\sin 2\psi](\gamma T + \lambda T'). \tag{12}$$

Moreover,

$$S = \frac{1}{2}\langle 3\cos^2\vartheta - 1\rangle, \quad S' = \frac{3}{2}\langle \sin^2\vartheta\cos 2\psi\rangle, \tag{13a}$$

$$T = \frac{1}{2}\langle \sin^2\vartheta\cos 2\varphi\rangle, \tag{13b}$$

$$T' = \frac{1}{2}\langle (1+\cos^2\vartheta)\cos 2\varphi\cos 2\psi - 2\cos\vartheta\sin 2\varphi\sin 2\psi\rangle. \tag{13c}$$

The scalar order parameters are constrained within the following bounds [25]:

$$-\frac{1}{2} \leqslant S \leqslant 1, \quad -(1-S) \leqslant S' \leqslant (1-S), \tag{14a}$$

$$-\frac{1}{3}(1-S) \leqslant T \leqslant \frac{1}{3}(1-S), \tag{14b}$$

$$-\frac{1}{3}\min\{2+S+3T+S', 2+S-3T+S'\} \leqslant T' \leqslant \frac{1}{3}\min\{2+S-3T+S', 2+S+3T-S'\}. \tag{14c}$$

Inequalities (14a) and (14b) are immediate consequences of Eqs. (13a) and (13b), whereas Eq. (14c), which narrows the admissible range $-1 \leqslant T' \leqslant 1$ predicted as a consequence of Eq. (13c), has been derived in [38] from a symmetry property.

Equations (13a) clearly show that even in the presence of a certain degree of alignment in the long molecular axis, which makes $S>0$, S' still vanishes if the short molecular axes are randomly distributed. Conversely, a certain degree of locking in the short axes distribution would contribute less to S' if the long axis is more aligned. Two different mechanisms contribute to build S': the locking of the short axes $(\boldsymbol{e},\boldsymbol{e}_\perp)$ and the widening of the cone described by the long axis $\boldsymbol{m}$ around the uniaxial director $\boldsymbol{e}_z$, which per se would decrease S. For this reason, in a uniaxial phase the growth of S' as the temperature decreases can be interpreted as a sign of effectiveness of the short axes locking compared with the long axis alignment and may also be accompanied by a temporary decrease of S. An alternative, geometric way to visualize this is offered by Eqs. (10) and (13a). It readily follows from them that

$$S' = \frac{3}{2}[\langle(\boldsymbol{e}\cdot\boldsymbol{e}_z)^2\rangle - \langle(\boldsymbol{e}_\perp\cdot\boldsymbol{e}_z)^2\rangle]. \tag{15}$$

An increase in S', which clearly measures the difference in the degree of alignment of the short molecular axes along the uniaxial director, is likely to be associated with a decrease in S, as this would widen the range of variability of both fluctuating quantities in Eq. (15).

Order parameters are often expressed as ensemble averages of symmetry-adapted combinations of Wigner rotation functions R^2_{00}, R^2_{20}, R^2_{02}, and R^2_{22} [15,18,32,42–45]. Here, to ease the comparison with other sources, we heed that these averages are related to S, T, S', and T' through the following equations:

$$\langle R^2_{00}\rangle = S, \quad \langle R^2_{20}\rangle = \sqrt{\frac{3}{2}}T, \tag{16a}$$

$$\langle R^2_{02}\rangle = \frac{1}{\sqrt{6}}S', \quad \langle R^2_{22}\rangle = \frac{1}{2}T'. \tag{16b}$$

The essential triangle in Fig. 2 is divided into three disjoint regions characterized by a different sequence of equilibrium phases traversed as the temperature decreases. Schematically, in such a sequence the isotropic, uniaxial, and biaxial phases are denoted by the symbols I, U, and B, respectively; a first-order transition is denoted by a dash and a second-order transition by an equal sign. Thus in $\mathsf{IC_2C_3}$ the equilibrium phase sequence is I-B, this meaning that as the temperature decreases an ensemble of biaxial molecules traverses both the isotropic and the biaxial phases, undergoing a first-order transition between the two. Similarly, in $\mathsf{C_2C_3C_1}$ the equilibrium phase sequence is I-U-B, and in $\mathsf{C_1C_3VO}$ it is I-U=B. As shown in [29], $\mathsf{C_2C_3}$ is a triple line, while $\mathsf{C_1C_3}$ is a tricritical line. Specifically, the points $\mathsf{C_1}$, $\mathsf{C_2}$, and $\mathsf{C_3}$ have the following coordinates $\mathsf{C_1} \simeq (0, 0.20)$, $\mathsf{C_2} \simeq (0, 0.22)$, and $\mathsf{C_3} = (\frac{5}{29}, \frac{19}{87})$.

IV. ORDER PARAMETER PROFILES

The phase diagram drawn in [25,28] for the Hamiltonians along OI and IT encompasses all the qualitative features of

the equilibrium phase sequences, and so it acquires a universal character. These phase sequences were obtained by applying the traditional minimum principle for the mean-field free energy to the fully attractive Hamiltonians and an appropriate minimax principle to the partly repulsive Hamiltonians [29]. To subject this minimax principle to further scrutiny, we studied in detail the order parameter profiles for two points, G and R, selected so as to explore the two subregions of OTV that behave differently under the permutation symmetry, namely, OTP and PTV (see Fig. 2). G is along the axis of the triangle PTV, halfway between the vertex T and the base PV; its coordinates are $G \simeq (0.33, 0.056)$. R is along PI, halfway between P and the intersection of PI with the arc OT; its coordinates are $R \simeq (0.16, 0.012)$.

The order parameter profiles have been obtained from a numerical bifurcation analysis of the equilibrium equations for $\mathcal{F}$, performed with the aid of MATCONT [46], a free software package which integrates into MATLAB [47]. In the parametrization (10) of the molecular orientation, these equilibrium equations read as

$$\frac{2}{3}(S + \gamma S') - \frac{Z_S}{Z} = 0, \tag{17a}$$

$$2(T + \gamma T') - \frac{Z_T}{Z} = 0, \tag{17b}$$

$$\frac{2}{3}(\gamma S + \lambda S') - \frac{Z_{S'}}{Z} = 0, \tag{17c}$$

$$2(\gamma T + \lambda T') - \frac{Z_{T'}}{Z} = 0. \tag{17d}$$

In Eqs. (17), Z_X denotes the partial derivative of the partition function Z with respect to the corresponding order parameter X; more precisely,

$$Z_X := \frac{\partial Z}{\partial X} = \int_0^{2\pi} \int_0^{2\pi} \int_{-1}^{1} h_X(u, \varphi, \psi) \exp(\beta g) du d\varphi d\psi, \tag{18}$$

where

$$h_S(u, \varphi, \psi) := \left(u^2 - \frac{1}{3}\right) + \gamma(1 - u^2)\cos 2\psi, \tag{19a}$$

$$h_T(u, \varphi, \psi) := (1 - u^2)\cos 2\varphi + \gamma h(u, \varphi, \psi), \tag{19b}$$

$$h_{S'}(u, \varphi, \psi) := \gamma\left(u^2 - \frac{1}{3}\right) + \lambda(1 - u^2)\cos 2\psi, \tag{19c}$$

$$h_{T'}(u, \varphi, \psi) := \gamma(1 - u^2)\cos 2\varphi + \lambda h(u, \varphi, \psi), \tag{19d}$$

and

$$h(u, \varphi, \psi) := (1 + u^2)\cos 2\varphi \cos 2\psi - 2u \sin 2\varphi \sin 2\psi.$$

Numerical evaluation of the integrals in Eq. (18) and of similar ones intervening in the bifurcation analysis is crucial to the success of our numerical strategy; therefore particular care has been taken in identifying the most appropriate computational method. The algorithm chosen is a combination of an $(m+1)\times(m+1)$-gridpoint composite trapezoidal rule for integration in φ and ψ, which is the method of choice for periodic functions integrated over an integer number of full periods [48], and an n-node Legendre-Gauss quadrature on the variable $u = \cos\vartheta$ [49].

In detail, for example, we approximate the function in Eq. (11) by

$$Z_{n,m} := 4 \sum_{i=1}^{n} \sum_{j=0}^{m} \sum_{k=0}^{m} w_i h_{kj} \exp[\beta g(u_i, \varphi_j, \psi_k)] \Delta^2, \tag{20}$$

where (u_i, w_i) are the Gaussian nodes and weights, respectively, for $i = 1, \ldots, n$; $\varphi_j = \frac{j\pi}{m}$ for $j = 0, \ldots, m$; $\psi_k = \frac{k\pi}{m}$ for $k = 0, \ldots, m$; $\Delta = \frac{\pi}{m}$, and

$$h_{kj} := \begin{cases} \frac{1}{4} & \text{if } (j = 0 \text{ or } j = m) \text{ and } (k = 0 \text{ or } k = m), \\ 1 & \text{if } j \neq 0, m \text{ and } k \neq 0, m, \\ \frac{1}{2} & \text{otherwise.} \end{cases} \tag{21}$$

Similar expressions are given by the numerical approximation for the functions in Eq. (18).

This algorithm proved to be faster than the MATLAB built-in quadrature codes in several tests for typical values of $(S, T, S', T', \beta, \gamma, \lambda)$; in such cases, $n = 24$ and $m = 16$ turned out to offer a good balance between speed and computation accuracy; relative errors in evaluating the integrals for typical values could be easily pushed to 10^{-10}, i.e., close enough to machine attainable accuracy. However, when a transition between phases occurs at low temperature, i.e., at large values of β, n and m need to be increased to improve accuracy in numerical evaluation of integrals. Other sources of error can limit the final accuracy of the results, such as tolerances for functions in MATCONT, computation of the free energy function, etc. We repeatedly tested the robustness of our computations against these sources of error.

A good test for the validity of the method is available. Since any phase state can be described by different sets of order parameters, these sets are equivalent under symmetry transformations corresponding to permutations of eigenvectors $(\boldsymbol{e}_x, \boldsymbol{e}_y, \boldsymbol{e}_z)$ of the order tensors in Eq. (6) [28,38]. Once a bifurcation point is detected on a solution branch, it may be continued on distinct branches, and yet equivalent through these symmetry transformations; different branches can then appropriately be recast, and so sent onto one and the same branch. As long as all branches match to one another in this transformation, at least in a fairly large neighborhood of the bifurcation point, no suspicion that numerical approximation is breaking the symmetry of the interaction should arise. In typical conditions, equivalent solutions were matched with accuracy less than 1% in the worst cases.

Nevertheless, even with poor numerical approximation of integrals, when spurious solutions may be found, the transition reduced temperatures as well as the order parameter values in their neighborhood are in agreement with the corre-

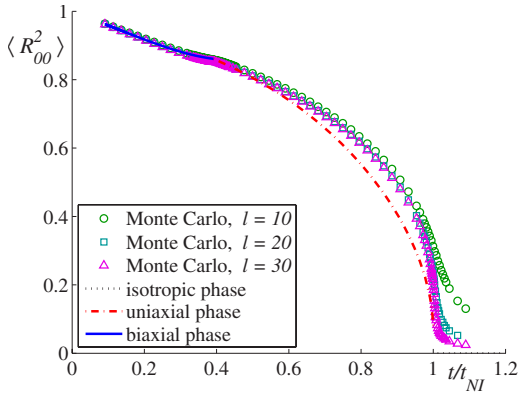

FIG. 3. (Color online) The ensemble average $\langle R^2_{00} \rangle = S$ of the Wigner function R^2_{00}, obtained by a mean-field analysis of the Hamiltonian represented by G (see Fig. 2), is plotted as a function of the ratio t/t_{NI}, where t is the absolute temperature and t_{NI} is the value of t that marks the nematic-to-isotropic transition. The corresponding Monte Carlo simulation results reported here and in the following figures were obtained with three sample sizes, $N=l^3$, with $l=10$, 20, and 30, correspondingly represented by circles ○, squares □, and triangles △. Temperatures were scaled to the nematic-isotropic transition temperature corresponding to the method employed. For all three Monte Carlo simulations, t_{NI} is the transition temperature computed for $l=30$ (see also Table I).

sponding values found with improved numerical computations to within a fairly good accuracy (less than 0.5%).

For the Hamiltonian represented by G, Figs. 3–6 show the order parameters $\langle R^2_{00} \rangle$, $\langle R^2_{20} \rangle$, $\langle R^2_{02} \rangle$, and $\langle R^2_{22} \rangle$ defined in Eqs. (16) as functions of the ratio t/t_{NI}, where t is the absolute temperature and t_{NI} is the value of t that marks the nematic-to-isotropic transition. Superimposed to these graphs are the points, here shown as circles, squares, and triangles, obtained

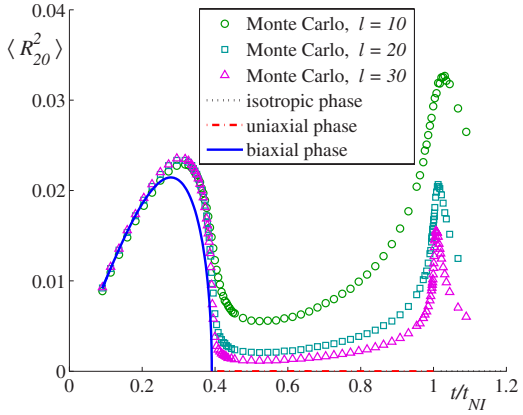

FIG. 4. (Color online) The ensemble average $\langle R^2_{20} \rangle = \sqrt{\frac{3}{2}} T$ of the Wigner function R^2_{20}, obtained by a mean-field analysis of the Hamiltonian represented by G (see Fig. 2), is plotted as a function of the ratio t/t_{NI}; superimposed to the plot are the corresponding points obtained from a Monte Carlo simulation for different sample sizes, $N=l^3$ (○, $l=10$; □, $l=20$; and △, $l=30$). (For more details, see the caption to Fig. 3.) Monte Carlo simulation results around the nematic-to-isotropic transition exhibit a "spurious" spike, whose height decreases with increasing sample size.

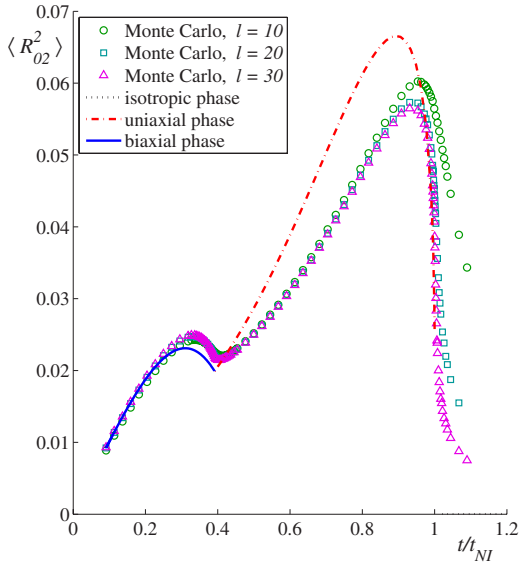

FIG. 5. (Color online) The ensemble average $\langle R^2_{02} \rangle = \frac{1}{\sqrt{6}} S'$ of the Wigner function R^2_{02}, obtained by a mean-field analysis of the Hamiltonian represented by G (see Fig. 2), is plotted as a function of the ratio t/t_{NI}; superimposed to the plot are the corresponding points obtained from a Monte Carlo simulation for different sample sizes, $N=l^3$ (○, $l=10$; □, $l=20$; and △, $l=30$). (For more details, see the caption to Fig. 3.) At the onset of the biaxial phase, both the mean-field analysis and the Monte Carlo simulation predict a *rebound* for this order parameter, which is a measure of the strength of attraction between the short molecular axes.

from a Monte Carlo simulation with different sample sizes: the total number of particles is $N=l^3$, with $l=10$, 20, and 30, respectively; the computational details are summarized in Sec. V. Though the values of t_{NI} computed through the mean-field approximation and the Monte Carlo simulation are different, once reduced to the same dimensionless temperature scale t/t_{NI}, the data obtained with the two methods are in remarkable agreement. Here for all three Monte Carlo simu-

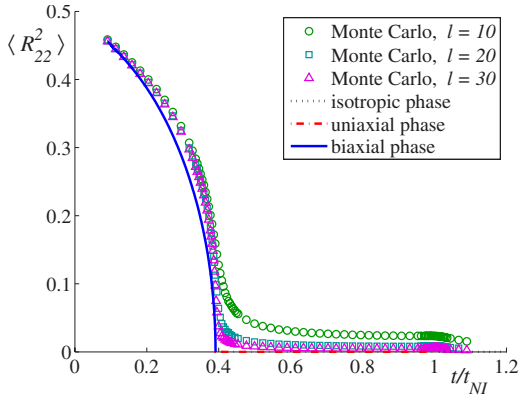

FIG. 6. (Color online) The ensemble average $\langle R^2_{22} \rangle = \frac{1}{2} T'$ of the Wigner function R^2_{22}, obtained by a mean-field analysis of the Hamiltonian represented by G (see Fig. 2), is plotted as a function of the ratio t/t_{NI}; superimposed to the plot are the corresponding points obtained from a Monte Carlo simulation for different sample sizes, $N=l^3$ (○, $l=10$; □, $l=20$; and △, $l=30$). (For more details, see the caption to Fig. 3.)

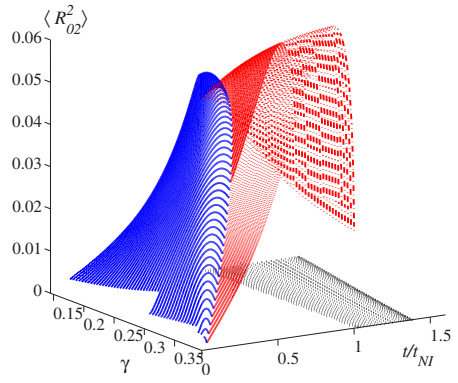

FIG. 7. (Color online) The ensemble average $\langle R^2_{02} \rangle = \frac{1}{\sqrt{6}} S'$ of the Wigner function R^2_{02}, obtained by a mean-field analysis of the Hamiltonians represented by several points in the essential triangle taken along the line through I and G below the tricritical line C_1C_3 (see the corresponding dashed line in Fig. 2). $\langle R^2_{02} \rangle$ is plotted as a function of t/t_{NI}, for several linearly spaced values of $\gamma = \frac{2}{5} - \frac{6}{5}\lambda$ ranging in [0.145, 0.395]. The rebound at the uniaxial-to-biaxial transition is a generic feature manifesting itself throughout the whole line selected, though with different strength.

lations t_{NI} is the transition temperature computed for the largest sample size ($l=30$).

In particular, one feature of the graphs for $\langle R^2_{02} \rangle$ in Fig. 5 strikes one's attention: as the temperature is reduced, at the onset of the biaxial phase, $\langle R^2_{02} \rangle$ starts growing again before decreasing towards zero, in agreement with inequalities (14a), as t/t_{NI} further decreases. In the light of our interpretation of the meaning of S', we take the growth of $\langle R^2_{02} \rangle$ at the biaxial transition as a qualitative measure of the strength of the short axes attraction. As expected, this growth is correlated with a dip in the graph of $\langle R^2_{00} \rangle$. Our understanding is that a higher uniaxial rebound at the biaxial transition witnesses a stronger biaxial effectiveness of the molecular interaction and should be associated with a deeper dip in the temperature profile of the uniaxial primary order parameter.

To see whether this feature is or is not peculiar to the point G, we extended our mean-field analysis along the direction IG up to the points where this intersects the tricritical line C_1C_3 and the base OV. The different graphs obtained for $\langle R^2_{02} \rangle$ are shown in Fig. 7: they clearly suggest that the uniaxial rebound at the biaxial transition may indeed be a generic feature of all interactions described by the subregion OC_1C_3V of the essential triangle.

A similar exploration was conducted for the point R: the corresponding order parameter plots are shown in Figs. 8–11, where they again appear contrasted against the Monte Carlo simulation illustrated in Sec. V. Figure 12 shows a collection of graphs for $\langle R^2_{02} \rangle$ taken on the section along IR. A uniaxial rebound at the biaxial transition is still appreciable here, though its degree has lessened compared with the section along IG.

Figures 7 and 12 support our claim that the uniaxial rebound is a property that accompanies the biaxial transition as soon as the interaction Hamiltonian fails to be represented by the border OIV of the essential triangle, where two scalar order parameters in general suffice to describe all equilibrium phases [25,28,38].

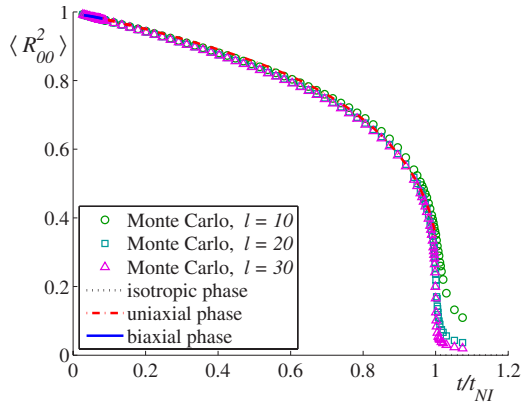

FIG. 8. (Color online) The ensemble average $\langle R^2_{00} \rangle = S$ of the Wigner function R^2_{00}, obtained by a mean-field analysis of the Hamiltonian represented by R (see Fig. 2), is plotted as a function of the ratio t/t_{NI}; superimposed to the plot are the corresponding points obtained from a Monte Carlo simulation for different sample sizes, $N=l^3$ (○, $l=10$; □, $l=20$; and △, $l=30$). (For more details, see the caption to Fig. 3.)

V. MONTE CARLO VALIDATION

The uniaxial rebound at the biaxial transition we described above appears as a universal feature accompanying the condensed phases predicted by the most general of Straley's interactions. This property was first predicted for the points G and R in the essential triangle representing the admissible interaction parameters, points for which the interaction Hamiltonian is partly repulsive, and so the minimax strategy must be applied to identify the equilibrium order parameters [29]. The suspicion could legitimately creep in a critical mind that this strategy may be responsible for the allegedly systematic uniaxial rebound, which could thus fail

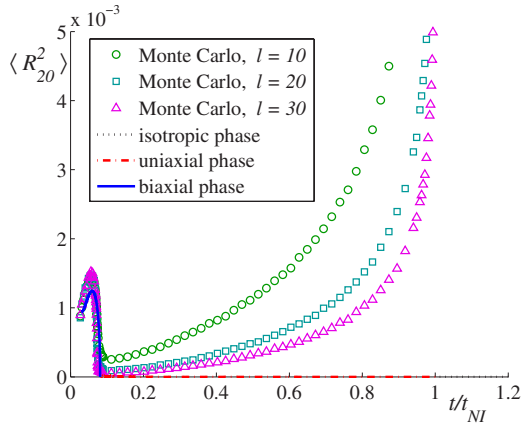

FIG. 9. (Color online) The ensemble average $\langle R^2_{20} \rangle = \sqrt{\frac{3}{2}} T$ of the Wigner function R^2_{20}, obtained by a mean-field analysis of the Hamiltonian represented by R (see Fig. 2), is plotted as a function of the ratio t/t_{NI}; superimposed to the plot are the corresponding points obtained from a Monte Carlo simulation for different sample sizes, $N=l^3$ (○, $l=10$; □, $l=20$; and △, $l=30$). (For more details, see the caption of Fig. 3.) Like in Fig. 4, Monte Carlo data show a spurious spike at the isotropic-to-nematic transition temperature, which is clearly a finite-size effect.

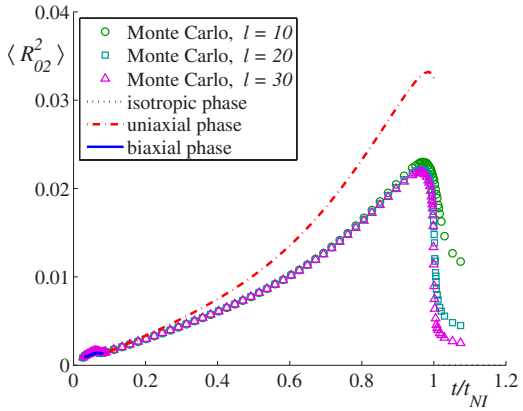

FIG. 10. (Color online) The ensemble average $\langle R_{02}^2 \rangle = \frac{1}{\sqrt{6}} S'$ of the Wigner function R_{02}^2, obtained by a mean-field analysis of the Hamiltonian represented by R (see Fig. 2), is plotted as a function of the ratio t/t_{NI}; superimposed to the plot are the corresponding points obtained from a Monte Carlo simulation for different sample sizes, $N=l^3$ (○, $l=10$; □, $l=20$; and △, $l=30$). (For more details, see the caption of Fig. 3.) The rebound at the onset of the biaxial phase, predicted both by the mean-field analysis and the Monte Carlo simulation, is less pronounced than in Fig. 5, but it is still present.

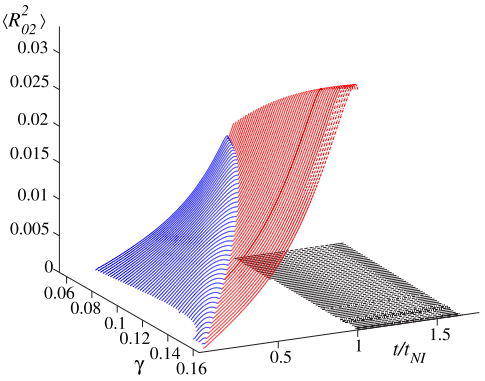

FIG. 12. (Color online) The ensemble average $\langle R_{02}^2 \rangle = \frac{1}{\sqrt{6}} S'$ of the Wigner function R_{02}^2, obtained by a mean-field analysis of the Hamiltonian represented by several points in the essential triangle taken along the line through I and R below the tricritical line C_1C_3 (see the corresponding dashed line in Fig. 2). $\langle R_{02}^2 \rangle$ is plotted as a function of t/t_{NI}, for several linearly spaced values of $\gamma = \frac{1}{6} - \frac{1}{2}\lambda$ ranging in [0.067, 0.16]. The rebound at the uniaxial-to-biaxial transition is a generic feature manifesting itself throughout the whole line selected, though with different strength.

to be real. To ensure that this feature is independent of our mean-field treatment, we performed a Monte Carlo simulation, which has only the interaction potential in common with the former treatment.

It was shown in [15] that, by standard geometric identities, Eq. (2) identically reduces to a combination of squares of the three scalar products involving corresponding unit vectors in the two molecular frames, $(\boldsymbol{e}, \boldsymbol{e}_\perp, \boldsymbol{m})$ and $(\boldsymbol{e}', \boldsymbol{e}'_\perp, \boldsymbol{m}')$. Here we consider a three-dimensional simple-cubic lattice Z^3 whose axes define the orthonormal basis $(\boldsymbol{e}_x, \boldsymbol{e}_y, \boldsymbol{e}_z)$. To each site μ, with coordinate vector $\boldsymbol{x}_\mu$, we associate a particle center of mass; the interaction potential H in Eq. (2) is restricted to nearest neighbors, involving molecules or sites labeled by μ and ν, respectively. Thus in the present setting,

$$H = -\epsilon\{P_2(\boldsymbol{m}_\mu \cdot \boldsymbol{m}_\nu) + 2\gamma[P_2(\boldsymbol{e}_{\perp\mu} \cdot \boldsymbol{e}_{\perp\nu}) - P_2(\boldsymbol{e}_\mu \cdot \boldsymbol{e}_\nu)] + \lambda[2P_2(\boldsymbol{e}_{\perp\mu} \cdot \boldsymbol{e}_{\perp\nu}) + 2P_2(\boldsymbol{e}_\mu \cdot \boldsymbol{e}_\nu) - P_2(\boldsymbol{m}_\mu \cdot \boldsymbol{m}_\nu)]\}, \tag{22}$$

where $\epsilon = \frac{2}{3} U_0$ and $P_2(x) := \frac{1}{2}(3x^2 - 1)$ is the second Legendre polynomial.

In a lattice situation, with a coordination number 6, the mean-field formalism changes by appropriate numerical factors [28]. In actual simulations we used a dimensionless temperature scale T^* which differs by a factor of 9 from the one in Eq. (9). Our conversion rule derives from the coordination number used for Monte Carlo simulations, as well as from an energy scale of the microscopic potential differing from the one used in the preceding sections by a factor $\frac{3}{2}$ (in turn, this was chosen so as to enforce a better compatibility with the Lebwohl-Lasher model). Thus the following mapping exists between the temperature scales:

$$T^* = \frac{9}{\beta}, \tag{23}$$

and both mean-field and simulation results were eventually converted to one and the same scale for comparisons. We list in Table I the critical temperatures in the scale T^* for both the I-U and the U=B phase transitions, computed within the mean-field and the Monte Carlo treatments for the points R and G in the essential triangle.

Calculations were carried on a periodically repeated cubic sample, consisting of $N=l^3$ particles, $l=10$, 20, and 30, and run in cascade, in order of increasing temperature; each cycle (or sweep) consisted of $2N$ Monte Carlo steps, including a

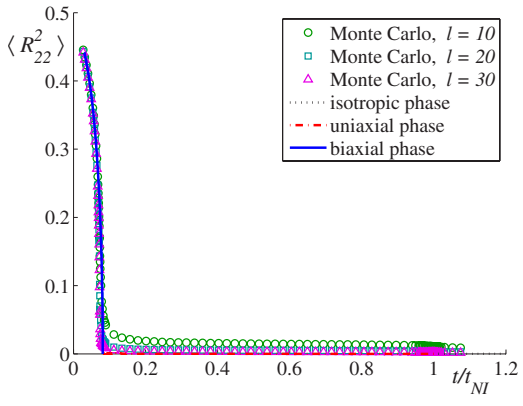

FIG. 11. (Color online) The ensemble average $\langle R_{22}^2 \rangle = \frac{1}{2} T'$ of the Wigner function R_{22}^2, obtained by a mean-field analysis of the Hamiltonian represented by R (see Fig. 2), is plotted as a function of the ratio t/t_{NI}; superimposed to the plot are the corresponding points obtained from a Monte Carlo simulation for different sample sizes, $N=l^3$ (○, $l=10$; □, $l=20$; and △, $l=30$). (For more details, see the caption of Fig. 3.)

TABLE I. Transition temperatures in the T^* scale computed with both mean-field and Monte Carlo treatments for the Hamiltonians described by the points R and G in the essential triangle (see Fig. 2). I-U denotes the first-order isotropic-to-uniaxial transition; U=B denotes the second-order uniaxial-to-biaxial transition. The Monte Carlo transition temperatures are computed for the largest sample size, $l=30$.

	I-U		U=B	
	Mean field	Monte Carlo	Mean field	Monte Carlo
R	1.365±0.004	1.117±0.002	0.111±0.003	0.080±0.001
G	1.560±0.001	1.101±0.002	0.610±0.004	0.428±0.005

sublattice sweep [50]. The simulation methodology closely followed other simulations of ours, e.g., [28], where further details can be found.

Equilibration runs took between 25 000 and 200 000 cycles, and production runs took between 200 000 and 800 000; macrostep averages for evaluating statistical errors were taken over 1000 cycles. Calculated thermodynamic quantities include mean potential energy per site U^* (where the asterisk means scaling by ϵ) and configurational specific heat per particle C^* (where the asterisk means scaling by k_B).

The four order parameters were obtained by averaging the appropriate symmetry adapted basis functions, and computed by analyzing a configuration every cycle, according to methodologies discussed in detail by other authors [18,22,43–45]; simulation results for the three sample sizes investigated here have been reported in Figs. 3–6 and 8–11.

Simulation results for the potential energy were largely insensitive to the sample size; simulation results for the specific heat exhibited a recognizable sample-size dependency only in the two transition ranges, where peaks could be seen growing higher and sharper upon increasing sample size.

Throughout the ordered phases, the sample-size dependencies of $\langle R_{00}^2 \rangle$ as well as $\langle R_{02}^2 \rangle$, i.e., of the two uniaxial order parameters, were found to saturate between $l=20$ and 30. At even higher temperatures, both observables were found to decrease with increasing sample sizes, and the temperature range where this change of scaling behavior took place was found to correspond to the high-temperature peak of the specific heat.

As for the two biaxial order parameters, both $\langle R_{20}^2 \rangle$ and $\langle R_{22}^2 \rangle$ remained independent of sample sizes up to a temperature range corresponding to the low-temperature peak of the specific heat, and then exhibited a pronounced decrease with increasing sample size above it; in this region, $\langle R_{20}^2 \rangle$ first decreased with increasing temperature, then it started increasing and reached a peak at a temperature corresponding to the loss of uniaxial order, and whose height kept decreasing with temperature; this behavior we interpret as a pure finite-size effect.

As far as we could check in the previous literature, the rebound behavior we are reporting here was not seen nor noticed; there seems to be a faint clue to it in some figures of [18].

VI. CONCLUSION

In the theoretical explorations of Straley's general interaction Hamiltonian for nematogenic biaxial molecules, it was often observed that only two scalar order parameters suffice to describe the whole sequence of equilibrium condensed phases experienced by an undistorted ensemble of biaxial molecules as the temperature is decreased [1,2,17,25,28]. It has recently been proved [29,38] that this property is actually the consequence of a symmetry enjoyed by Straley's interaction Hamiltonian H in Eq. (2) when the parameters (γ,λ) are chosen along the sides OI and IV of the essential triangle in Fig. 2. A similar order parameter reduction has long been known for the Hamiltonian H_0 in Eq. (4) represented by the arc OT along the parabola corresponding to London's dispersion forces approximation [1,2].

Our attempt to find further symmetries that would justify an order parameter reduction in the interior of the essential triangle has so far failed. Here we endeavored to select a generic macroscopic feature that would be common to the whole class of Straley's microscopic interactions corresponding to the points in the interior of the essential triangle. We think we identified this feature in the temporary increase of the order parameter S', related to the ensemble average $\langle R_{02}^2 \rangle$ of a Wigner symmetry-adapted function, which represents the uniaxial component of the biaxial order tensor **B** in Eq. (7b).

In all our mean-field calculations, we found that as the temperature is decreased, S', already decreasing in the uniaxial phase, abruptly starts to increase again at the biaxial transition. Such a uniaxial rebound is temporary, as S' eventually decreases to zero, but it seems to persist for all interactions in the interior of the essential triangle. A dip in the temperature profile of S is systematically associated with the rebound of S'.

Our analysis was applied to both fully attractive and partly repulsive Hamiltonians, that is, to both the Hamiltonians described by the region above the arc OT in Fig. 2 and those described by the region below it. While the global minimum of the mean-field free energy exists for the former Hamiltonians, it does not for the latter. Our computational approach was correspondingly based on minimum and minimax principles [29].

A Monte Carlo simulation was also conducted for two partly repulsive Hamiltonians and it confirmed our mean-field predictions, including the uniaxial rebound at the biaxial transition. The results of these simulations, which are not doctored by any mean-field treatment, were contrasted with our mean-field predictions. The qualitative agreement we achieved between these different approaches should be regarded as a tribute to the validity of the minimax principle.

We conclude that the uniaxial rebound at the biaxial transition can be regarded as a generic signature of Straley's interaction: within this theory, its absence could only be explained by the further symmetries associated with either sides OI and IV of the essential triangle.

Finally, an experimental test of the prediction reported here requires measuring the appropriate order parameters; we recall that in some cases it has been possible to estimate both $\langle R_{00}^2 \rangle$ and $\langle R_{02}^2 \rangle$ by combining experimental data obtained by

different techniques [51–53]. On the other hand, we cannot forget the caveat of [53], page 89: "It should be stated from the outset that there really are no experimental methods that provide unambiguous absolute values for the order parameters."

ACKNOWLEDGMENTS

F.B. and E.G.V. are indebted to E. C. Gartland, Jr. for precious suggestions and enlightening discussions on the mean-field bifurcation analysis adopted in this paper, during our common stay at the IMA, Institute for Mathematics and its Applications, University of Minnesota, Minneapolis, MN, USA, where part of this work was done. The Monte Carlo calculations were carried out, among other machines, on workstations, belonging to the Sezione di Pavia of Istituto Nazionale di Fisica Nucleare (INFN); allocations of computer time by the Computer Centre of Pavia University and CILEA (Consorzio Interuniversitario Lombardo per l' Elaborazione Automatica, Segrate, Milan), as well as by CINECA (Centro Interuniversitario Nord-Est di Calcolo Automatico, Casalecchio di Reno, Bologna), are gratefully acknowledged.

[1] M. J. Freiser, Phys. Rev. Lett. **24**, 1041 (1970).
[2] M. J. Freiser, Mol. Cryst. Liq. Cryst. **14**, 165 (1971).
[3] L. J. Yu and A. Saupe, Phys. Rev. Lett. **45**, 1000 (1980).
[4] G. R. Luckhurst, Thin Solid Films **393**, 40 (2001).
[5] L. A. Madsen, T. J. Dingemans, M. Nakata, and E. T. Samulski, Phys. Rev. Lett. **92**, 145505 (2004).
[6] B. R. Acharya, A. Primak, and S. Kumar, Phys. Rev. Lett. **92**, 145506 (2004).
[7] K. Severing and K. Saalwächter, Phys. Rev. Lett. **92**, 125501 (2004).
[8] K. Severing, E. Stibal-Fischer, A. Hasenhindl, H. Finkelmann, and K. Saalwächter, J. Phys. Chem. B **110**, 15680 (2006).
[9] K. Merkel, A. Kocot, J. K. Vij, R. Korlacki, G. H. Mehl, and T. Meyer, Phys. Rev. Lett. **93**, 237801 (2004).
[10] K. Neupane, S. W. Kang, S. Sharma, D. Carney, T. Meyer, G. H. Mehl, D. W. Allender, S. Kumar, and S. Sprunt, Phys. Rev. Lett. **97**, 207802 (2006).
[11] G. R. Luckhurst, Nature (London) **430**, 413 (2004).
[12] G. R. Luckhurst, Angew. Chem., Int. Ed. **44**, 2834 (2005).
[13] Y. Galerne, Phys. Rev. Lett. **96**, 219803 (2006).
[14] L. A. Madsen, T. J. Dingemans, M. Nakata, and E. T. Samulski, Phys. Rev. Lett. **96**, 219804 (2006).
[15] S. Romano, Physica A **337**, 505 (2004).
[16] J. P. Straley, Phys. Rev. A **10**, 1881 (1974).
[17] N. Boccara, R. Mejdani, and L. De Seze, J. Phys. (Paris) **38**, 149 (1976).
[18] F. Biscarini, C. Chiccoli, P. Pasini, F. Semeria, and C. Zannoni, Phys. Rev. Lett. **75**, 1803 (1995).
[19] J. N. Israelachvili, *Intermolecular and Surface Forces* (Academic Press, London, 1992).
[20] B. Tjipto-Margo and G. T. Evans, J. Chem. Phys. **94**, 4546 (1991).
[21] P. I. C. Teixeira, A. J. Masters, and B. M. Mulder, Mol. Cryst. Liq. Cryst. Sci. Technol., Sect. A **323**, 167 (1998).
[22] M. P. Allen, Liq. Cryst. **8**, 499 (1990).
[23] P. J. Camp and M. P. Allen, J. Chem. Phys. **106**, 6681 (1997).
[24] P. J. Camp, M. P. Allen, and A. J. Masters, J. Chem. Phys. **111**, 9871 (1999).
[25] A. M. Sonnet, E. G. Virga, and G. E. Durand, Phys. Rev. E **67**, 061701 (2003).
[26] B. Bergersen and P. Palffy-Muhoray, Liq. Cryst. **3**, 347 (1988).
[27] G. De Matteis and E. G. Virga, Phys. Rev. E **71**, 061703 (2005).
[28] G. De Matteis, S. Romano, and E. G. Virga, Phys. Rev. E **72**, 041706 (2005).
[29] F. Bisi, E. G. Virga, E. C. Gartland, Jr., G. De Matteis, A. M. Sonnet, and G. E. Durand, Phys. Rev. E **73**, 051709 (2006).
[30] L. Longa, P. Grzybowski, S. Romano, and E. Virga, Phys. Rev. E **71**, 051714 (2005).
[31] B. M. Mulder, Liq. Cryst. **1**, 539 (1986).
[32] B. Mulder, Phys. Rev. A **39**, 360 (1989).
[33] M. P. Taylor, Liq. Cryst. **9**, 141 (1991).
[34] B. M. Mulder, Mol. Phys. **103**, 1411 (2005).
[35] R. Rosso and E. G. Virga, Phys. Rev. E **74**, 021712 (2006).
[36] W. Maier and A. Saupe, Z. Naturforsch. A **14A**, 882 (1959) [Translated into English in T. J. Sluckin, D. Dunmur, and H. Stegemeyer, *Crystals that Flow* (Taylor and Francis, London, 2004), pp. 381–385].
[37] R. Rosso, Liq. Cryst. (to be published).
[38] G. De Matteis, F. Bisi, and E. G. Virga, Continuum Mech. Thermodyn. (published online on 21 February 2007).
[39] N. N. Bogolubov, Jr., *A Method for Studying Model Hamiltonians* (Pergamon Press, Oxford, 1972).
[40] N. N. Bogolubov, Jr., B. I. Sadovnikov, and A. S. Shumosky, *Mathematical Methods of Statistical Mechanics of Model Systems* (CRC Press, Boca Raton, FL, 1994).
[41] M. A. Osipov and A. S. Shumovskii, Teor. Mat. Fiz. **46**, 125 (1981) [Theor. Math. Phys. **46**, 83 (1981)].
[42] C. Chiccoli, P. Pasini, F. Semeria, and C. Zannoni, Int. J. Mod. Phys. C **10**, 469 (1999).
[43] C. Zannoni, in *The Molecular Physics of Liquid Crystals*, edited by G. R. Luckhurst and G. W. Gray (Academic Press, London, 1979), Chaps. 3 and 9.
[44] C. Zannoni, in *Advances in the Computer Simulations of Liquid Crystals*, edited by P. Pasini and C. Zannoni, NATO Science Series, Vol. C 545 (Kluwer, Dordrecht, 2000), Chap. 2.
[45] G. R. Luckhurst, in *Physical Properties of Liquid Crystals: Nematics*, edited by D. A. Dunmur, A. Fukuda, and G. R. Luckhurst (INSPEC, London, 2001), Chap. 2.1.
[46] See http://www.matcont. ugent. be/matcont. html
[47] MATLAB is a registered trademark of The MathWorks, Inc., http://www.mathworks.com
[48] E. Isaacson and H. B. Keller, *Analysys of Numerical Methods*, reprint ed. (Dover Publications, New York, 1994).
[49] F. B. Hildebrand, *Introduction to Numerical Analysis*, reprint ed. (Dover Publications, New York, 1994).

[50] R. Hashim and S. Romano, Int. J. Mod. Phys. B **13**, 3879 (1999).
[51] R. Alben, J. R. Mc Coll, and C. S. Shih, Solid State Commun. **11**, 1081 (1972).
[52] G. Vertogen and W. H. de Jeu, *Thermotropic Liquid Crystals, Fundamentals* (Springer, Berlin, 1988).
[53] S. Picken, in *Physical Properties of Liquid Crystals: Nematics* (Ref. [45]), Chap. 2.2.
[54] It should be noticed that, in keeping with other investigations and with mean-field treatments, we are considering here interaction potentials that are isotropic in orientation space, i. e., only depending on mutual orientations between particles.
[55] Strictly speaking, spatial average means here averaging a more general pair potential with respect to interparticle separation.